Supplementary Information — Hydrodynamic Spin-Pairing and Active Polymerization of Oppositely Spinning Rotors

Mattan Gelvan, Jonathan Kirpitch, Yahav Lavie, Artyom Chirko, Noa Israel, and Naomi Oppenheimer
Department of Physics and Astronomy and the Center for the Physics and Chemistry of Living Systems, Tel-Aviv University.
(Dated: October 10, 2025)

A mixed population of rotors at intermediate Reynolds numbers self-assembles into active polymers. Here, we provide additional details of the experimental setup, including the structure of the rotors, the 3D printing designs, the tracking procedures, and the electric circuit. We show that when one rotor is pinned, the gyromer is formed around it. We analyze the mean gyromer length and standard deviation as a function of time for higher concentrations of rotors. We elaborate on the theoretical solution of two rotors of varying spin, including a scaling analysis of the inertial term. We show the Particle Image Velocimetry setup and the resulting flows as a function of height, which are not symmetric — flows at the height of the propeller decay faster. We show that capillary forces between rotors exist but are negligible compared to forces resulting from their activity. We also show that inertial forces deviate from the theoretical predictions at small distances. We provide additional details about the simulation, including details on the periodic boundary conditions and analysis of the addition of positional and angular velocity noise to the stability of gyromers.

I. EXPERIMENTAL SETUP AND DATA ANALYSIS

The rotors consist of a brushless motor (80 rpm in air) and a battery housed within a 3D-printed cylindrical shell. The motor model was designed using "Tinkercad" with a circular profile of radius $a = 1.8\,cm$ and height 7.5 cm, featuring a square base compatible with the motor attachment. The model was printed using a 3D printer (Bumba lab-1-Carbon) with PLA+ 1.75 mm filament in the desired color, with a print density set to 70%. Similarly, a stand to securely hold the battery (LIR2477) in place on the motor was printed. The printed models can be seen in Fig 1. To build the motor's electrical circuit, we attached the wires of the motor using alligator clips to facilitate easy switching and charging. The clips were attached to the battery terminals housed in the 3D-printed stand. The motor's direction of rotation was determined by the connection of the wire clamps to the battery terminals. The batteries were charged at a constant current profile, using a TENMA DC power supply (model 72-13370), connected to the batteries in a circuit as shown below. Each battery voltage was set to $\sim 4.1V$ before the start of each run. It is important to ensure that all batteries have a uniform voltage to avoid differences in angular velocity between the motors. The motor was glued to the 3D-printed shell using hot glue, ensuring the motor was sealed so that the silicone oil does not penetrate. Thin 3D-printed belts were positioned around the rotors to minimize friction with each other and the bounding walls. A 3D-printed propeller was attached to the bottom pin of the motor to ensure that the motor and propeller counter-rotated and both were immersed in oil to ensure similar resistance.

The rotors were placed in a round bath of silicone oil [diameter 60 cm, height 9.5 cm, with viscosities of either $\mu = 1\,\mathrm{Pa\cdot s}$, $\beta \sim 0.3$ (high viscosity), or $\mu = 0.06\,\mathrm{Pa\cdot s}$, $\beta \sim 5$ (low viscosity), and density $\rho = 10^3\,\mathrm{kg/m^3}$]. To minimize the boundary effects of the bath, we added semicircles along the entire edge of the bath as an inverse-flower-like shape. These were designed to ensure that rotors near the edge returned to the bath instead of being attracted to the boundary. This unique shape was designed by principles outlined in Refs. [1, 2]. The semicircle models and the supporting legs for the bath boundary were designed in "Inkscape" and laser-cut from perspex (thickness: 0.5 cm) using the Beambox laser cutter.

After placing the rotors in the silicone oil bath, it is crucial to ensure that they are balanced to avoid precession. Each rotor was carefully balanced using Plasticine (see Fig. 1c). We have marked each rotor with a green off-center dot in order to identify and analyze the spin of the rotors.

The experiment was continuously monitored from above using a Sony camera (α7s_3, lens FE 4/24-105 G-OSS), capturing snapshots at one-second intervals. We tracked the trajectory of each rotor using Python using the OpenCV library. After identifying each rotor's center in each frame, the picture was cropped according to the dimensions of the rotor to identify the off-centered green dot. Then, using simple vector analysis, we have calculated the change in the angle between consecutive frames,

$$\Omega_{j(t=i)} = \cos^{-1}\left(\frac{\tilde{\mathbf{r}}_{j(t=i)} \cdot \tilde{\mathbf{r}}_{j(t=i+1)}}{\tilde{r}_{j(t=i)}\tilde{r}_{j(t=i+1)}}\right) + \pi k \qquad (1)$$

where $\Omega_{j(t)}$ is the spin of the jth rotor, $\tilde{\mathbf{r}}_{j(t)}$ is the off-centered green dot vector of the jth rotor in its center of mass frame, and k represents the number of half spins made between each consecutive frame (we made sure that between each consecutive frame k=0). The rotors' spin was calculated to be approximately 7 rpm ($\Omega \approx 0.7$ rad/s) at the start of each experiment. Once the batteries started to fail after ~ 2 hours, the rotor's spin slowly decayed to zero. The spin of the rotors over time was smoothed using Statsmodel LOWESS function using a fraction of 0.2.

We have conducted and analyzed tens of experiments

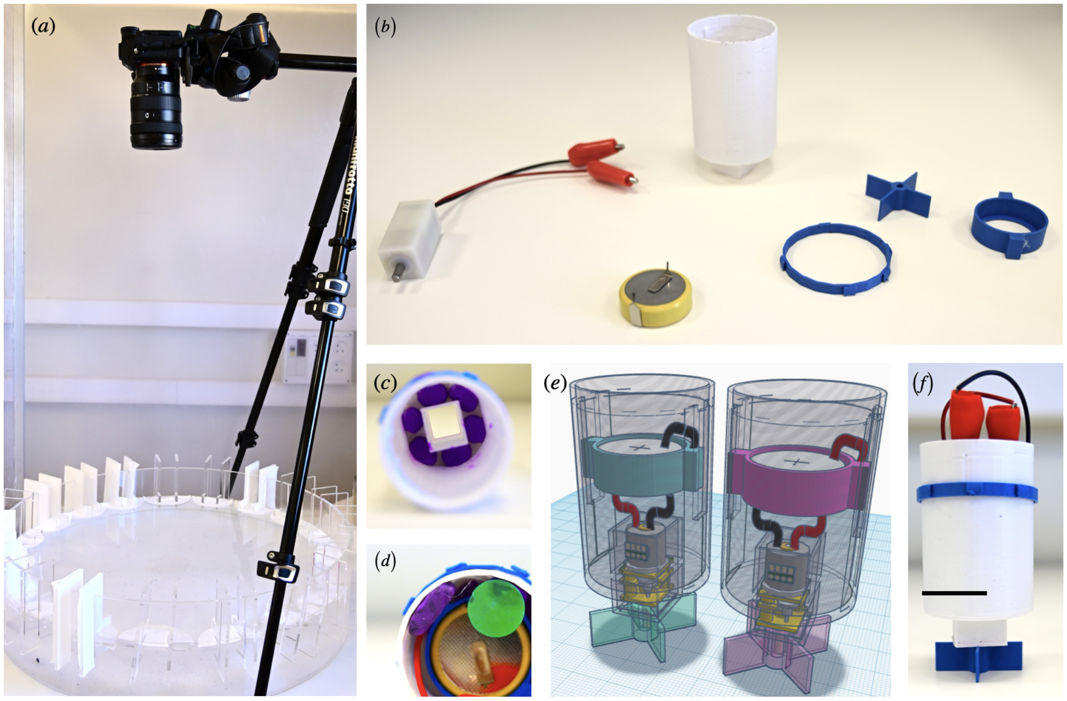

Supplementary Figure 1. (a) The silicone bath with the inverse flower shape boundaries, above it positioned a camera (this setup is the same for both the high and the low viscosity baths). (b) The components of the rotors - the propeller, belt, battery and battery house, a motor with positive(red) and negative(black) connections. (c) The Plasticine arrangement to stabilize the rotor before inserting the electrical circuit, viewing from above the rotor. (d) The rotor from above after inserting the electrical circuit, and placing the off-centered green dot to analyze the spin, and additional Plasticine to stabilize and prevent precession. (e) Sketch of the rotors and the electrical circuit inside them. (f) The final rotor before placing in the silicone bath (scale bar of 1.8cm).

of up to 20 rotors. Most experiments began with rotors clustered at the center of the bath, allowing us to observe the resulting structure formations. The majority of these experiments involved an even number of rotors, half rotating clockwise (in pink) and the other half counter-clockwise (in cyan). Some trials included an odd number of rotors, resulting in one poplulation having an additional rotor. We also investigated pre-designed initial conditions such as initializing the experiments with rotors arranged in a straight gyromer, a circular ring or as two facing pairs.

In order to analyze the gyromers' length and frequency of appearance during the experiment and the simulation, we used Depth-First Search algorithm. We have defined neighboring rotors once their distance from one center to another is less than $2.5a$. In order to avoid counting formations which are not chains a threshold was imposed such that a legitimate gyromer is one that agrees with the following: It has at least one rotor that has only 1 neighbor, there are more rotors with 2 neighbors than with 3 neighbors, there is no rotor with 4 neighbors, and the formation lasted for at-least 10 frames. This rules will not allow formations like closed rings, lattices, and mix formations of large lattices connected to a chain to be counted, moreover the time threshold of 10 frames binds the counted formations to have some stability.

In the high viscosity bath ($\mu = 1\,\mathrm{Pa{\cdot}s}$, $\beta \sim 0.3$), the gyromers, once formed, consistently increase their gyration length to a maximum, eventually stabilizing in straight lines. Deviations from this behavior occur when the precession of the rotors increases (mainly due to unbalanced rotors) or due to significant noise in the spin of the rotors. In the low viscosity bath ($\mu = 0.06\,\mathrm{Pa \cdot s}$, $\beta \sim 5$), due to higher inertial forces and surface deformation, the formed gyromers are more curved, and branched gyromers may appear in addition to ring formations as transients (see Fig. 4 in main text). In this regime we calculated the radius of gyration R_g as discussed in the main text.

For the 7 rotors $\mathrm{R_g} \in [3, 4.2]$ where we observe that the gyromer first starts with small $R_g \sim 3$ and increases its length until stabilizing on $R_g \sim 4$. For the 14 rotors run $\mathrm{R_g} \in [4.4, 5.5]$ where most of the time it maintained $R_g \sim 5.2$. These values can be compared with the radius of gyration of straight-line gyromers which yields for 5 rotors $R_g \sim 3$, for 7 rotors $R_g \sim 4.3$ and for 14 rotors $R_g \sim 8.3$. The above discussion shows the fluctuating nature of the gyromers in the low viscosity bath.

In Fig. 2, an example is shown for a typical small numbered gyromer in the low viscosity bath. In this specific run, we localized one of the rotors using perspex rods that were used to redirect it to the center of the bath while still allowing it to rotate. The center was marked

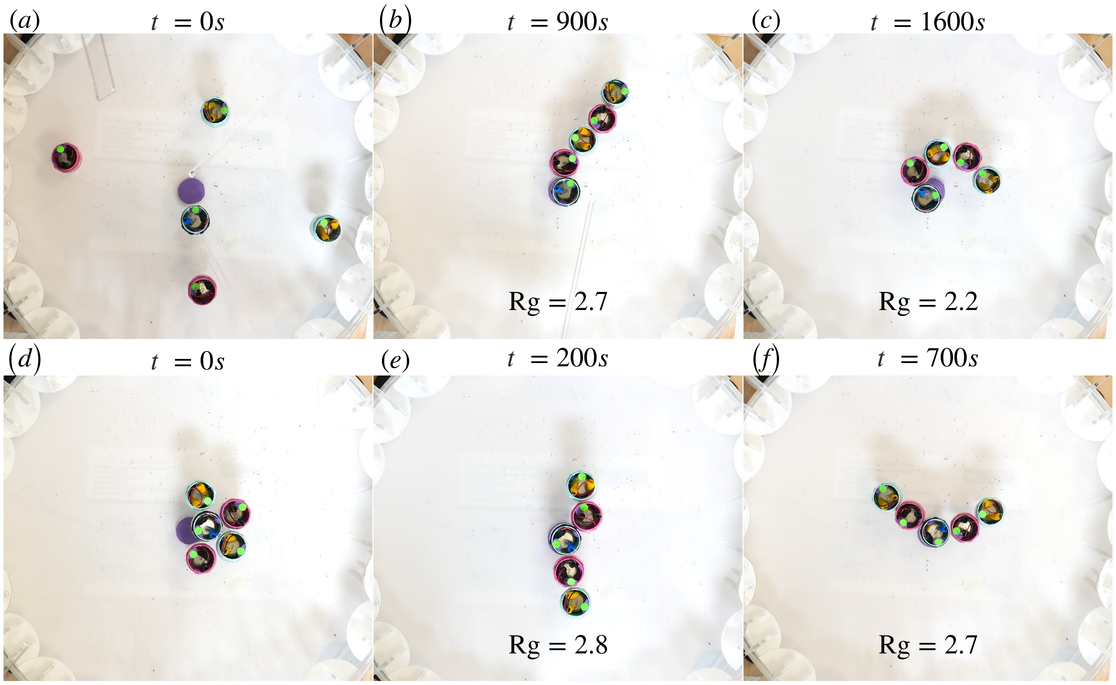

Supplementary Figure 2. Five-rotor experiment with one manually spatially pinned rotor in the low viscosity bath. (a)-(c) Starting from a spacious configuration, while the middle rotor is pinned to the center, a gyromer is subsequently formed where the pinned rotor is positioned at one of its ends. The plastic rods used to pin the rotor can be seen in (a) and (b). (d)-(f) Starting from a centered random aggregate, a gyromer is formed with the pinned rotor at its center.

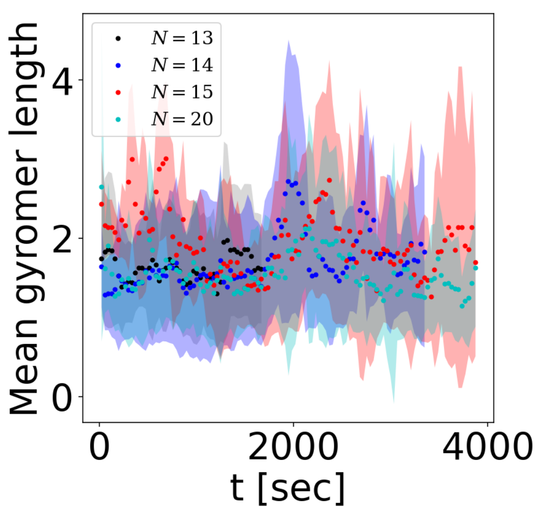

Supplementary Figure 3. Mean gyromer length in units of rotor diameter as a function of time. Results from four experiments $[N \in (13, 14, 15, 20)]$ in $\mu = 1\text{Pa}\cdot\text{s}$, $\beta = 0.3$. Each dot is an average over 40s with an overlap of 5s. The standard deviation is shaded on top. Source data are provided as a Source Data file.

with purple plasticine as can be seen in Fig. 2a. The resulting formed gyromer can be seen in Fig. 2b, and 2c. One of the edges is of the pinned rotor. A second run is presented in Fig. 2e and 2f, where the resulting gyromer has the pinned rotor at its center. The calculated dimensionless radius of gyration $\mathrm{R_g}$ is shown for each formation.

For the calculation of the two rotors experiments, we have analyzed the orbit, $\dot{\theta}$, using Eq. 1 with the relative distance between the rotors, $\mathbf{r}_{(t=i)}$, instead of $\tilde{\mathbf{r}}_{j(t=i)}$. Because the dynamic of the orbit is very slow, less than a single pixel in the consecutive frame, we averaged over ten frames taking $\dot{\theta}_{(t=i)}/10$ and $\mathbf{r}_{(t=i+10)}$ instead of simply one as before and again making sure $k = 0$.

For calculating the angular velocity of the odd-rotor gyromers, we used the relative distance between the middle rotor and its two furthest rotors in the chain $\mathbf{r}_{1/2(t=i)}$. The average angular velocity in each frame $\bar{\dot{\theta}}_{(t=i)}$ was calculated using the average of the two $\dot{\theta}_{1/2(t=i)}/10$, using Eq. 1 with $\mathbf{r}_{1/2(t=i+10)}$, same as for the two-rotor case.

We characterize the dynamics of the rotors by measuring the average gyromer length and the standard deviations as a function of time (see Fig.3). After identifying the stabilization of the mean gyromer length, we concluded that a steady state has been reached. From that point, we calculated the temporal mean gyromer length taken over the total number of frames. The results are shown in Fig.4b in the main text.

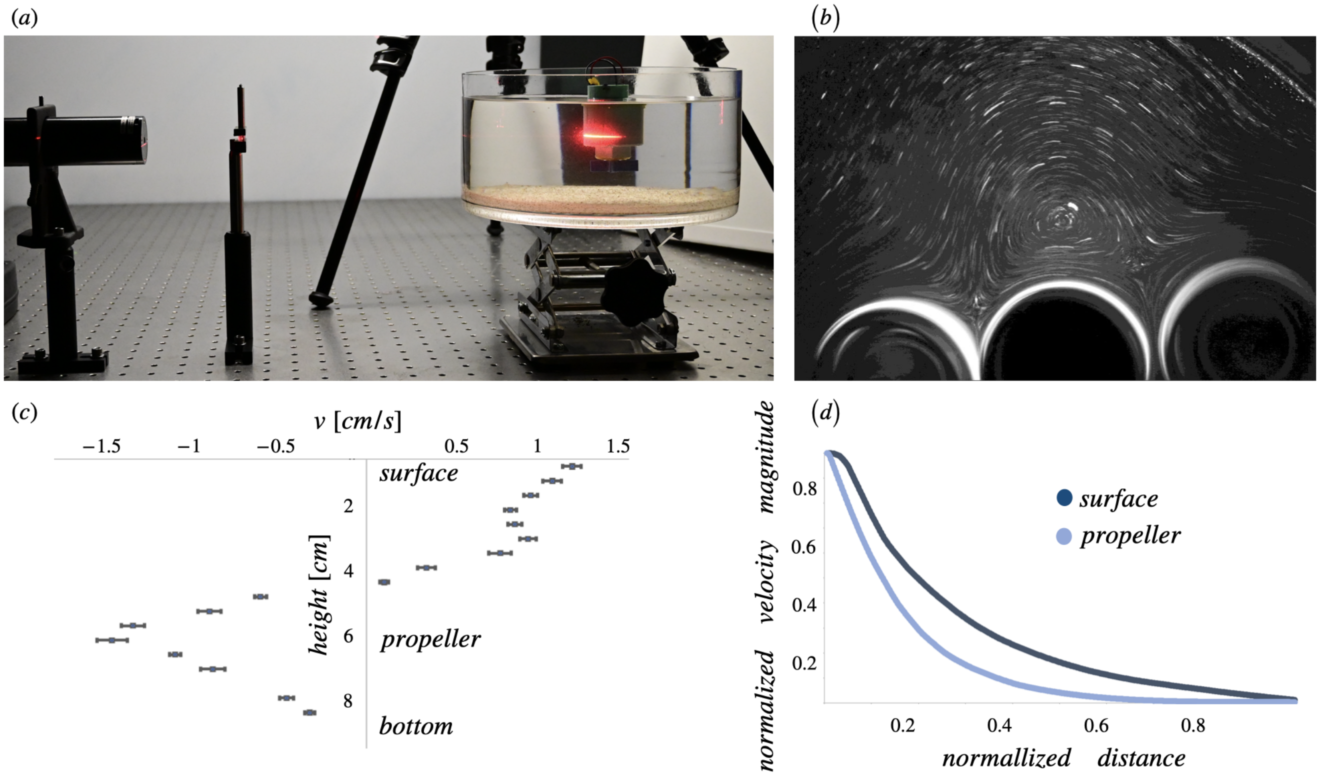

Supplementary Figure 4. (a) PIV experimental setup. A laser emits toward a cylindrical lens of $3.9mm$ focal length, resulting a thin laser plane. Small silicon oil bath with $\mu = 1\text{Pa}\cdot\text{s}$, positioned $\sim 40cm$ away from the lens, and placed over a jack to enable heights change. A camera positioned above the bath, continuously montior the small particles in order to identify the flow created in the bath. (b) PIV analysis image showing the flow created at the surface from the dynamics of three rotors — minus, plus, minus. (c)-(d) Analysis of one clockwise rotor flow. (c) The velocity magnitude, at a distance of, $r = 1.1a$ ($\sim 2cm$) from the rotor's center, as a function of height. Positive (negative) velocity magnitude value regards clockwise (counter-clockwise) flow. (d) The velocity magnitude as a function of the distance, r, showing the differences between the surface flow and the flow at the propeller height. The values have been normalized such that the maximum value of v and r is one and for the distance, zero value is when $r = a$ ($1.8cm$). It can be seen that the rotors do not act as a perfect rotor-dipoles in the Z-axis. Source data are provided as a Source Data file.

II. PIV MEASUREMENTS

Particle Image Velocimetry (PIV) of the flow field was performed using Thorlabs-HNL050L laser and PIVlab software (Fig. 4). The laser emitted towards a cylindrical lens with focal length of 3.9mm (Thorlabs-LJ1598L1) achieving a wide thin laser plane ($\sim$ 6.4mm height). The flow field was obtained from the scattered impurities placed in the fluid. The experiment was continuously monitored from above using a Sony camera ($\alpha 7s3$, lens FE 2.8/90 MACRO G-OSS), filming the small bath with $\mu = 1\text{Pa}\cdot\text{s}$ at 25 frames per second. Several experiments were conducted using a single rotor placed in the middle of the bath while changing the laser plane compared to the rotor such that different heights of the flow could be analyzed. For each height, we analyzed the velocity magnitude along a line in the $\hat{r}$ direction. The resulting flow field is tangential to the $\hat{\theta}$ direction, while positive (negative) values regard counter-clockwise (clockwise) direction flow. A plot of the velocity magnitude at $r = 1.1a$ ($\sim$ 2cm), from the rotor's center, as a function of height ($\hat{z}$ direction) is shown in Fig. 4c. We have also analyzed the decay of the speed with respect to the distance from the rotor's center, r. We compared the decay of flow at the surface to the decay of flow at the height of the propeller ($\sim 6cm$ below the surface), as can be seen in Fig. 4d. We can see that the lower part of the flow decays faster compared to the surface flow due to the proximity to the bottom surface. The results show the anti-symmetry along the Z-axis, which is the reason why the flow does not resemble a torque dipole, and the upper surface dominates the behavior. It explains why when observing the behavior of two same-sign rotors, we got a typical angular velocity of, $\dot{\theta} \propto 1/r^3$, which is a result of a velocity of a single rotor decaying as $u_s \propto 1/r^2$. This is the flow of a rotating disk in an infinite viscous fluid. The velocity of a single torque dipole rotor decays faster as $u_{s,dipole} \propto 1/r^3$, which is not the case here.

III. THEORETICAL MODEL

As we outline in the main text, a single rotor far from boundaries stays static. When placed in a bath of other rotors, it is advected by the flow created by all other rotors. By accounting for a single neighboring rotor, the resulting angular velocity of the first in the viscous regime, $\dot{\theta}$, is given by

$$\dot{\theta} \propto \Omega_2/r^3, \tag{2}$$

where Ω_2 is the spin of the neighboring rotor and r is the distance between the two rotors. When inertial effects are included, a second rotor adds a correction to the viscous flow (u_s), giving a lift force resembling the Magnus effect. In order to account for such effects, one needs to solve the Naiver-Stokes equations under a small but finite Reynolds number for a spinning disk. For simplicity, we can solve the equations for a sphere that gives the same scaling. The full perturbated solutions of the velocity, force, and pressure for a spinning and propagating sphere, in the case of small, not negligible, Reynolds number, as a result of inertial effects, is explicitly shown in the thesis work [3]. The leading order correction of the force, created by a spinning sphere, propagating in a constant velocity, u^{∞}, is given by

$$\mathbf{F}_m = \pi\rho a^3 \mathbf{u}^{\infty} \times \mathbf{\Omega}, \tag{3}$$

where ρ is the density of the fluid, a is the sphere's radius, Ω is the spin of the sphere, and F_m, is the leading correction force which can be thought of as a Magnus-like force. In our system, the propagating velocity of the first sphere is not due to a constant background velocity but due to the second rotor. For a counter-clockwise rotating neighboring sphere, we take ($\mathbf{\Omega}_2 = \Omega_2\hat{z}$), using Eq. 2, we can show that the shear rate created by one sphere on the second is [4],

$$\mathbf{u}^{\infty} \propto (a\Omega_2)\frac{a^3}{r^3}\hat{\theta} \tag{4}$$

where a minus sign will be given for a clockwise spinning neighboring sphere. By substituting Eq. 4 in Eq. 3, the inertial correction of the flow, u_i, (using that in the over-dumped limit $F \propto \mu u a$) for the first disk, spinning counter-clockwise, $\mathbf{\Omega}_1 = \Omega_1\hat{z}$, is

$$\mathbf{u_i} \propto \frac{\rho\Omega_1\Omega_2 a^6}{\mu r^3}\hat{r}. \tag{5}$$

For two spinning disks in the same (opposite) direction, the resulted Magnus force is repulsive (attractive).

The velocity of the jth disk, $\mathbf{u}_j$, is given by the total flow created by all other disks (accounting for the viscous flow with its inertial correction while assuming linearity in this regime). In complex notation $z_j = x_j + iy_j$, it is given by

$$\dot{z_j} = \sum_k iC_s\Omega_k\frac{z_j - z_k}{|z_j - z_k|^s} + C_i\Omega_j\Omega_k\frac{z_j - z_k}{|z_j - z_k|^m}, \tag{6}$$

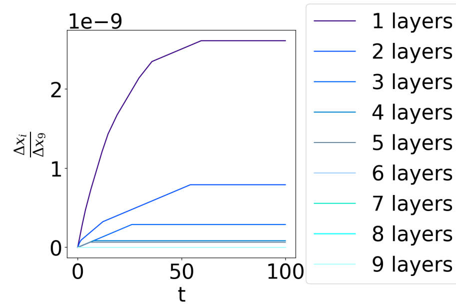

Supplementary Figure 5. Relative error in the distance between two rotors in identical conditions, for simulations with periodic boundary conditions, compared across several layers of repeated windows with a window size $L = 8$, and rotors at an initial distance $r = 4$. Source data are provided as a Source Data file.

where Ω_j is the jth rotor own spin, and C_s and C_i are constants. For completeness we kept the power laws s and m general. Using the scaling in Eq. 5 and Eq. 1 in the main text gives $s = 3$ and $m = 4$.

We now solve analytically Eq. 6 for two rotors. Taking $\Omega_1 = \Omega$ and $\Omega_2 = \gamma\Omega$ gives

$$\begin{aligned} \dot{z_1} &= \left(iC_s\gamma\Omega|z_1 - z_2|^m + C_i\gamma\Omega^2|z_1 - z_2|^s\right)\frac{z_1 - z_2}{|z_1 - z_2|^{s+m}} \\ \dot{z_2} &= \left(iC_s\Omega|z_1 - z_2|^m + C_i\gamma\Omega^2|z_1 - z_2|^s\right)\frac{z_2 - z_1}{|z_1 - z_2|^{s+m}} \end{aligned} \tag{7}$$

We now define $\eta = z_1 - z_2 = re^{i\theta}$, where r is the distance between the rotors and θ the angle between them. Substituting η in the equations above,

$$\dot{\eta} = \left[iC_s(1+\gamma)\Omega r^m + 2C_i\gamma\Omega^2 r^s\right]\frac{\eta}{r^{s+m}}. \tag{8}$$

Notice that $dr^2/dt = \dot{\eta}\overline{\eta} + \eta\dot{\overline{\eta}}$ where $\overline{\eta}$ is the complex conjugate. Then by using Eq. 8 we find the radial velocity between the two rotors,

$$\frac{dr^2}{dt} = 2r\frac{dr}{dt} = r^{2-m}4C_i\gamma\Omega^2 \tag{9}$$

giving a distance between the two rotors to the mth power

$$r^m = 2mC_i\gamma\Omega^2 t + r^m_{t=0}. \tag{10}$$

Substituting Eq. 10 in Eq. 8 gives

$$\frac{d\eta}{dt} = \eta\left(\frac{2C_i\gamma\Omega^2}{2mC_i\gamma\Omega^2 t + A} + i\frac{(1+\gamma C_s\Omega)}{(2mC_i\gamma\Omega^2 t + A)^{s/m}}\right), \tag{11}$$

where we have marked $A = r^m_{t=0}$. Solving Eq. 11 results in,

$$\eta = B\, r \exp\left[i\frac{C_s}{C_i}\frac{1+\gamma}{2\gamma\Omega(m-s)}r^{m-s}\right], \tag{12}$$

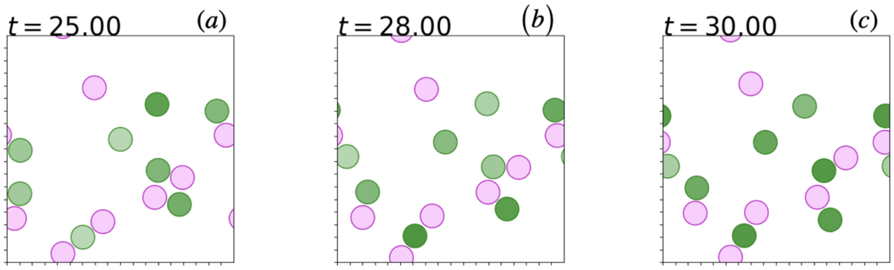

Supplementary Figure 6. Images from a noisy numerical simulation showing the destabilizing effect of noise on lattice formation. Three different snapshots are taken from a simulation with $\beta = 2$. For $\beta = 2$, a ring of four alternating rotors is stable. Here a lattice is observed at $t = 25$, the introduction of noise destabilizes it, allowing the ring to open up to a Gyromer at subsequent frames. $N_\Omega = 0.5$ is the angular-velocity noise level used here, meaning rotational velocities vary in the interval $[0.5, 1.5]$. $N_p = 0.002$ is the positional noise level. The transparency of each rotor is determined by the magnitude of its rotation velocity — the more transparent it is, the slower it rotates.

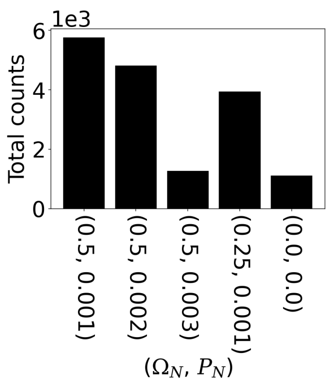

Supplementary Figure 7. Total count of non-trivial (length greater than 3 rotors) Gyromers in a simulation with $\beta = 2$. All simulations had identical initial conditions, and only vary in noise power. Adding some noise increases the prevalence of Gyromers, but adding too much can destabilize Gyromers as well, as seen in the (0.5, 0.003) case. We hypothesize that the required noise level to destabilize aggregates is dependent on β, but leave further investigation of this connection for future work. Source data are provided as a Source Data file.

where $B = \eta_{t=0}$. Now writing $\eta = re^{i\theta}$ in Eq. 12 gives the solution for the angle between the rotors

$$\theta = \frac{C_s}{C_i} \frac{1+\gamma}{2\gamma\Omega(m-s)} r^{m-s} - i\ln(B). \tag{13}$$

Taking the derivative of Eq. 13 and using Eq. 9 we finally obtain

$$\dot{\theta} = \frac{(\gamma+1)C_s\Omega}{r^s}. \tag{14}$$

We can summarize the two equations given in the main text

$$r^m = 2mC_i\gamma\Omega^2 t + A$$
$$\dot{\theta} = \frac{(\gamma+1)C_s\Omega}{r^s}.$$

The importance of these two equations lays in the ability to experimentally find s, and m independently of one another. As shown and outlined in the main text, for the high viscosity (low viscosity) bath with $\mu = 1\mathrm{Pa}\cdot\mathrm{s}$ ($\mu = 0.06\mathrm{Pa}\cdot\mathrm{s}$), we have conducted five (three) different experiments with two rotors of the same sign, to find explicitly the exponents, s and m. A log-log plot of $\dot{\theta}$ as a function of r, resulted in a linear behaviour with the slope equal to $-s$, which gave $s = 3.095 \pm 0.056$ (3.29 ± 0.20 for the low viscosity case). Analyses of r^m as a function of time, taking m in the range of $[1, 8]$ were made, giving the best R^2 test values for $m = 4$, with $R^2 = 0.9817 \pm 0.0024$ (for the low viscosity experiments we get $R^2 = 0.9856 \pm 0.0049$). Taking the log-log plot of r^4 as a function of time resulted in a slope of 1.037 ± 0.083 (0.92 ± 0.14). In the low viscosity case ($\mu = 0.06\,\mathrm{Pa}\cdot\mathrm{s}$), inertia is more significant; there is a strong and fast repulsion between rotors. Therefore, the orbiting is much less dominant. This immediately led to a much more noisy data than the one received from the high viscosity case with $\mu = 1\mathrm{Pa}\cdot\mathrm{s}$, as can be seen above.

IV. NUMERICAL SIMULATIONS

Molecular Dynamics simulations were written in Python using a fifth-order (in free-space) and a second-order (with periodic boundary conditions) Runge-Kutta scheme. Equation 6 with $s = 3$ and $m = 4$ was non-dimensionalized with position $z \to z/a$, spin $\Omega_i \to \Omega_i/\Omega_0$, and time $t \to (C_s\Omega_0/a^3)t$, where Ω_0 is the typical spin of the rotors (in the simulations taken to be 1). The position of the jth rotor is thus given by

$$\dot{z_j} = \sum_k i\Omega_k \frac{z_j - z_k}{|z_j - z_k|^3} + \beta\Omega_j\Omega_k \frac{z_j - z_k}{|z_j - z_k|^4}, \tag{15}$$

where $\beta = C_i\Omega_0/(aC_s)$ gives a typical nondimensional number that signifies the importance of inertial effects compared to viscous ones and is proportional to the

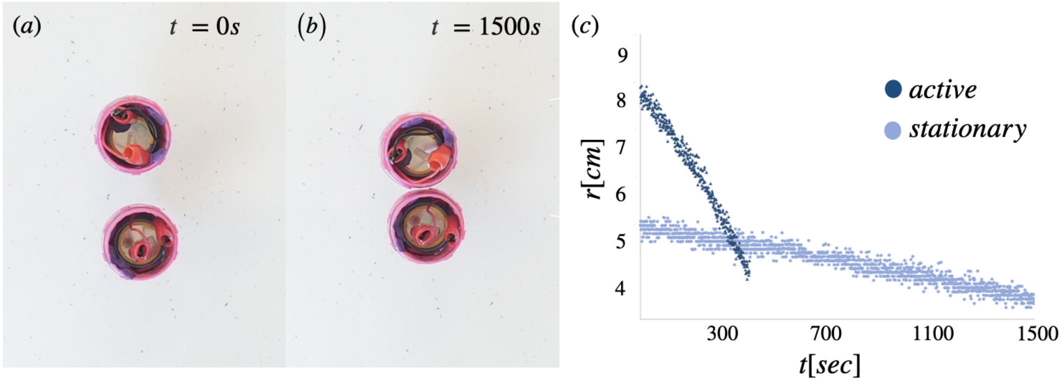

Supplementary Figure 8. (a) Two stationary un-active rotors, placed in the high viscosity bath, attracting each other due to the fluid surface tension (Cheerios effect). (b) After $\sim 25 minutes$ the two bodies attached. (c) Plot of the the distance between the two rotors as a function of time, showing the differences of the attraction magnitude in case of two stationary rotors compared to two active plus and minus rotors attraction. The mean velocity magnitude between the active to stationary attraction is about ~ 10 times greater. Source data are provided as a Source Data file.

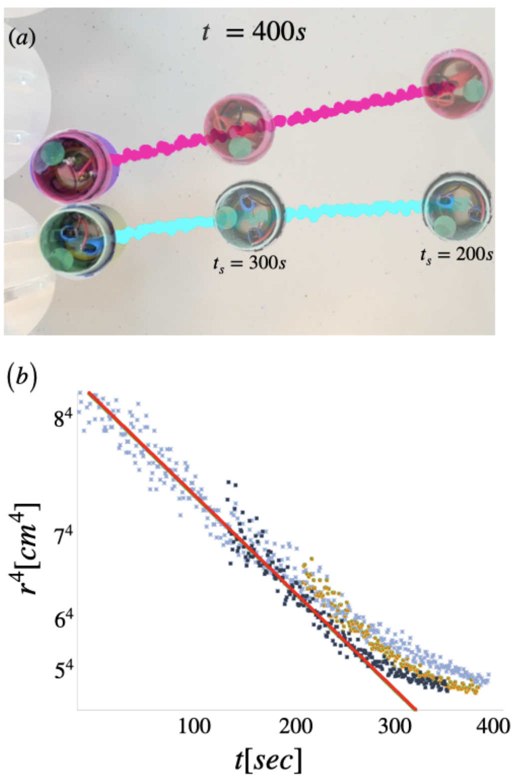

Supplementary Figure 9. (a) Two rotors tracking analysis of different signs — plus and minus in the high viscosity bath. At the end of the dynamics the attraction magnitude drastically reduced. (b) Distance to the fourth as a function of time for two rotors of different signs. Overlay of three different experiments, and a linear trend line marked in red showing the linearly starting behaviour disrupted approximately once $r < 3a$. Source data are provided as a Source Data file.

Reynolds number. We have tested values of β ranging from 0.01 to 1000. Typical behaviors are reported in the main text. The spin of the rotors is $\Omega_i = \pm 1$. In some runs we have added a small Gaussian noise at each time step, typically adding 10% noise. The timestep we used is $dt = 10^{-5}$. Soft-core steric interactions between particles were included in the form of purely repulsive harmonic springs, such that if the particles are closer than $2a$ the force is zero. Thus, the force between particle i and j is $\boldsymbol{f}_{ij}^{\text{steric}} = -w_s(1 - 2a/r_{ij})\mathbf{r}_{ij}$, where r_{ij} is the distance between the particles, and $w_s = 5 \cdot 10^4$ is the strength of the interaction. If $r_{ij} > 2a$, we set $\boldsymbol{f}_{ij}^{\text{steric}} = 0$. In addition, if particles draw closer than $r_{ij} = 1.8a$ we set the radial interaction between particles to zero, i.e. we state that steric interaction must cancel the attractive force. We found that this later condition helps to stabilize the simulation and increase timestep dramatically without changing the behavior.

We have tested several boundary conditions: (1) rotors in free-space, (2) rotors confined by a circular disk, (3) rotors in an inverse flower shape, imitating the experimental set-up, and (4) rotors on a torus (periodic boundary). The boundaries were set as soft-core repulsive potentials, similar to the interactions between the particles. We did not include hydrodynamic interactions between the particles and the wall, and indeed we see deviations from the experiments at the boundary. Although interaction with the circular disk appeared similar to the experiments in which particles are attracted to the boundary, the inverse flower design resulted in a different behavior — in the experiments, the inverse flower design results in apparent repulsion from the boundary, in the simulations, particles were attracted to the boundary. For the periodic boundary conditions, since the interactions are long-ranged, we would ideally have infinite copies of the simulation area. Since this is impossible computationally, we surround the core simulation area with several layers of copies. The velocities scale as a combination of r^{-2} and r^{-3}. Therefore, the Stokes interactions, which decay as $1/r^2$ give the most considerable contribution.

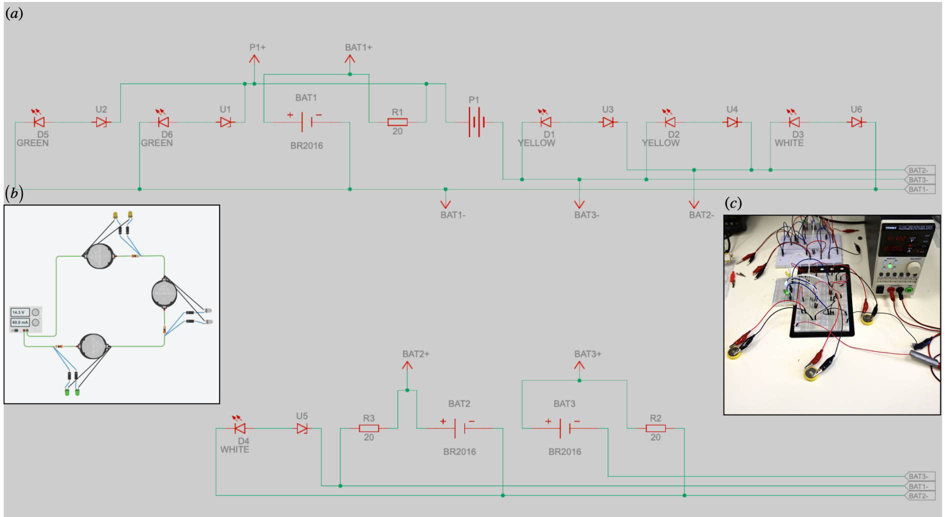

Supplementary Figure 10. (a) Sketch of the electrical circuit designed to recharge the batteries (LIR2477) in a constant current charge profile. The power supply configured to supply $0.06[A]$ and the batteries were connected to each other in a row. Once one of the batteries reached 4.0V, the current started to flow in the bypass circuit pre-designed with two identical zener diodes and two led diodes for identification. (b) Illustration of the circuit. (c) The bread board picture, showing the alligator clips for the connection of the batteries.

When simulating a mixed population of positive and negative rotors, the joint far-distance interactions decay as a derivative of $1/r^2$, thus they scale as $1/r^3$. We therefore expect that a small number of layers will suffice (rather than using approaches such as Ewald summation, spectral methods, or the force coupling method). To be extra strict, we tested empirically simulations of two same-sign rotors at a separation of $r = 4$, which have a far-distance decay of $1/r^2$ using an increasing number of layers. The results can be seen in Fig. 5. For each case, we compare the positions of the rotors with their positions with 9 layers. We see that the relative error gives negligible corrections for this window size ($L = 8$), that saturate over time. Beyond three layers the relative error is less than $1e^{-9}$. We therefore have chosen to work with simulations of between 3 and 5 layers.

To obtain the experimental value β, we used Eqs. 10 and 14 to determine the values of C_i *and* C_s, which were extracted from the graphs presented in Fig. 2 in the main text. This results in $\beta = 0.309 \pm 0.058$ for the high viscosity bath and $\beta = 4.71 \pm 0.42$ for the low viscosity bath.

Each dot in Fig.4C in the main text represents a set of parameters used for an experiment or simulation. The classification of a run is based on the most prominent formation type (disordered/ring/gyromer/lattice) when examining the largest formations in the run. For example, if 50% of the time the largest formation in the run was identified as a gyromer (regardless of its actual length), the run will be classified as a gyromer. In cases that were inconclusive, we performed several iterations using different initial conditions and used the majority vote. A disordered result is obtained when dimers and monomers are the dominant formation. We identify formations based on adjacency in clusters. To qualify as a ring, each rotor in a formation must have exactly two neighbors. To be classified as a gyromer, a formation needs to have at least one end (a rotor with a single neighbor), no rotors with 4 neighbors (surrounded on all sides), and overall more rotors with two neighbors than three. Everything else is classified as an aggregate, with special cases for a ring of size 4 (a square) and a 2-by-3 lattice, to only be considered aggregates. The mixed cases (half blue, half red) are cases where we obtained stable coexistence of gyromers and aggregates, with the division between the rotors being highly dependent on the initial conditions. Those were marked manually.

Noisy simulations. To better simulate the physical experiment, we added positional and angular-velocity noise to the simulations. Where in the experiment, noise simply arises due to precession of an un-fully buoyant rotor or from changes in the batteries voltage. The noise added in both cases was white. We found that a small amount of noise increases the prevalence of Gyromers, primarily by destabilizing crystal structures as seen in Fig. 6. The quantitative effect of noise on Gyromer prevalence can be seen in Fig. 7.

V. DEVIATIONS FROM THEORY

Deviations of the simulations from the experimental results can be due to several causes as outlined in the main text. Here we explore two such causes — (1) The Cheerios effect and (2) Boundary layer effect.

The Cheerios effect. Capillary forces between two rotors exist as they exist between all rigid bodies that deform a fluid interface causing the particles to attract or repel. This effect, which is termed The Cheerios effect, is due to the surface tension of the liquid. In our system, it leads to attraction between the rotors. However, this attraction is much weaker and leads to velocities which are an order of magnitude smaller. We made several experiments in the high viscosity bath with two rotors which are not active and do not spin, and compared them to active rotors. We also tested interaction with the boundary. Analyzing the resulting velocity led to $u_c \sim 0.001[cm/s]$. This is about ~ 10 times smaller than the approximate radial velocity due to the inertial hydrodynamic force, u_i, as can be seen in Fig. 8c.

Boundary Layer effect. The inertial correction to the flow is the far distance first approximation of the flow, meaning that it takes into account only the term of $u_s \propto O(r^{-3})$ (the Stokes flow created by a spinning disk or a sphere). In our system, it is clearly not the case for close neighbors in a gyromer or a dimer where there are additional corrections of at least $O(r^{-4})$ to the flow as a result of the proximity of the two rotors — acting as rotor dipoles in the fluid surface plane. In addition, inertial effects are smaller in proximity to the rotor's surface where stick boundary conditions apply. Several experiments of two rotors of opposite signs have been conducted to examine specifically the close neighboring behavior (in the high viscosity bath). As can be seen in Fig. 9a, when the rotors get close to one another, the change in the distance between them decreases at a slower rate. There is a smaller slope to their approach. Overlay analysis of three different experiments of the distance between the rotors to the fourth power, r^4, as a function of time, is given in Fig. 9b. The starting behavior is linear, presented in the red trend line, as predicted for the two same sign rotors experiments we showed, resulting in $m = 4$. However, it can be seen that once $r \approx 3a$ ($5.4cm$), the behavior qualitatively changes. The theoretical model no longer gives accurate predictions and there are deviations from the experimental results.

[1] E. Arbel, N. Oppenheimer, Y. Lahini, and M. Y. B. Zion, A mechanical origin of cooperative transport, arXiv preprint arXiv:2402.05659 (2024).

[2] M. Casiulis, E. Arbel, Y. Lahini, S. Martiniani, O. Naomi, and M. Y. Ben Zion, arXiv:2409.04618.

[3] D. Beck, Magnus force acting upon a rotating sphere passing in an incompressible viscous flow, (2018).

[4] B. A. Grzybowski, X. Jiang, H. A. Stone, and G. M. Whitesides, Dynamic, self-assembled aggregates of magnetized, millimeter-sized objects rotating at the liquid-air interface: Macroscopic, two-dimensional classical artificial atoms and molecules, Physical Review E **64**, 011603 (2001).